ACS APPLIED MATERIALS & INTERFACES

Research Article

Cite This: ACS Appl. Mater. Interfaces 2019, 11, 865−879

www.acsami.org

CdTe Quantum Dot-Functionalized P25 Titania Composite with Enhanced Photocatalytic NO_2 Storage Selectivity under UV and Vis Irradiation

Merve Balci Leinen,[†] Didem Dede,[‡] Munir Ullah Khan,[†] Mustafa Çağlayan,[†,⊥] Yusuf Koçak,[†] Hilmi Volkan Demir,*[,‡,§,∥] and Emrah Ozensoy*[,†,‡]

[†]Department of Chemistry, [‡]UNAM—National Nanotechnology Research Center and Institute of Materials Science and Nanotechnology, and [§]Department of Electrical and Electronics Engineering and Department of Physics, Bilkent University, Ankara 06800, Turkey

[∥]School of Electrical and Electronic Engineering, School of Physical and Mathematical Sciences, and School of Materials Science and Engineering, Nanyang Technological University, Singapore 639798, Singapore

Supporting Information

ABSTRACT: Composite systems of P25 (titania) functionalized with thioglycolic acid (TGA)-capped CdTe colloidal quantum dots (QDs) were synthesized, structurally characterized, and photocatalytically tested in the photocatalytic NO_x oxidation and storage during $NO(g) + O_2(g)$ reaction. Pure P25 yielded moderate-to-high NO conversion (31% in UV-A and 40% in visible (vis)) but exhibited extremely poor selectivity toward NO_x storage in solid state (25% in UV-A and 35% in vis). Therefore, P25 could efficiently photooxidize $NO(g) + O_2(g)$ into NO_2; however, it failed to store photogenerated NO_2 and released toxic $NO_2(g)$ to the atmosphere. CdTe QD-functionalized P25 revealed a major boost in photocatalytic performance with respect to pure P25, where NO conversion reached 42% under UV-A and 43% under vis illumination, while the respective selectivity climbed up to 92 and 97%, rendering the CdTe/P25 composite system an efficient broad-band photocatalyst, which can harvest both UV-A and vis light efficiently and display a strong NO_x abatement effect. Control experiments suggested that photocatalytic active sites responsible for the $NO(g) + O_2(g)$ photooxidation and formation of NO_2 reside mostly on titania, while the main functions of the TGA capping agent and the CdTe QDs are associated with the photocatalytic conversion of the generated NO_2 to the adsorbed NO_x species, significantly boosting the selectivity toward solid-state NO_x storage. Reuse experiments showed that photocatalytic performance of the CdTe/P25 system can be preserved to a reasonable extent with only a moderate decrease in the photocatalytic performance. Although some decrease in the photocatalytic activity was observed after aging, CdTe/P25 could still outperform P25 benchmark photocatalyst. Increasing CdTe QDs loading from the currently optimized minuscule concentrations could be a useful strategy to increase further the catalytic lifetime/stability of the CdTe/P25 system with only a minor penalty in catalytic activity.

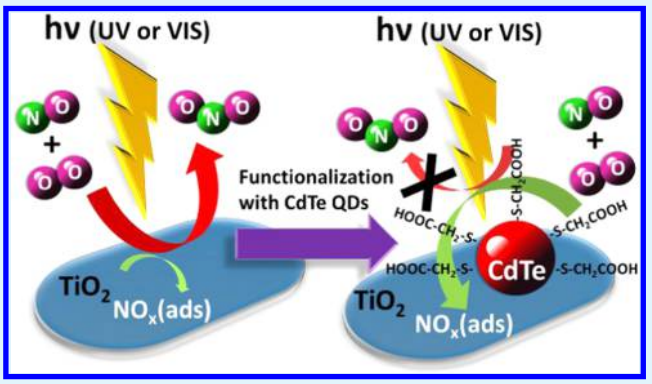

KEYWORDS: *CdTe colloidal quantum dots, titanium dioxide, photocatalytic NO_x abatement*

1. INTRODUCTION

Air pollution caused by CO, SO_2, NO_x (e.g., NO, NO_2, and N_2O), particulate matter, and unburned hydrocarbons is one of the major global environmental challenges.[1,2] During the combustion of nitrogen-containing species in air, nitrogen can be oxidized and form NO(g). With further oxidation of NO, other more toxic NO_x species, including NO_2, can also be formed. Nitrogen oxides are highly reactive and harmful air pollutants, which can lead to acid rain, photochemical smog, formation of secondary air pollutants, and ozone depletion.[3,4] Photocatalytic $NO_x(g)$ oxidation and storage (PHONOS) is an environmentally friendly and sustainable $DeNO_x$ technique, in which airborne NO_x is oxidized and stored on photocatalyst surface in the form of solid-state nitrate species,[5−8] which can readily exploit abundant solar radiation under ambient conditions (i.e., at room temperature). Photocatalysis for $DeNO_x$ processes is typically initiated by the photogenerated electron−hole pairs. The presence of adsorbed molecular water together with dissociated water species, such as surface hydroxyl groups, is crucial for the photocatalytic $DeNO_x$ processes.[9] Adsorbed water molecules on the surface of the photocatalyst can also function as an electrolyte.[10] Titanium

Received: October 16, 2018
Accepted: December 11, 2018
Published: December 11, 2018

DOI: 10.1021/acsami.8b18036
ACS Appl. Mater. Interfaces 2019, 11, 865−879

dioxide (TiO_2) is the most widely used semiconductor for the photocatalytic decomposition of gaseous and liquid-phase pollutants.[11,12] TiO_2 is abundant, cost-efficient, chemically and thermally stable, hydrophilic, and also is capable of oxidizing organic/inorganic species.[13,14] Photocatalytic activity of TiO_2 is governed by a multitude of complex chemical, physical, and electronic properties, including the phase/crystal structure, specific surface area (SSA), crystallite size, defect structure/density, work function, and electronic band gap.[15−20] In acidic medium, anatase and brookite phases of TiO_2 are metastable, while the most stable form of TiO_2 is the rutile phase. In basic medium, anatase is more stable than rutile and brookite phases.[21] TiO_2 has bulk band gap energy of 3.2 eV for the anatase and 3.0 eV for the rutile.[22] This wide band gap of TiO_2 limits the efficient exploitation of the solar spectrum outside the ultraviolet (UV) region. There have been numerous attempts to enhance the photocatalytic efficiency of TiO_2, e.g., via nonmetal doping,[23,24] metal doping,[25−28] and surface modifications with polymers.[29−31] In this study, a semiconductor CdTe-based colloidal quantum dot (QD) component was introduced to the catalyst architecture so that the photogenerated electrons from the QDs can be injected to the conduction band of TiO_2, whereas the photogenerated holes in the valence band of TiO_2 are transferred to the valence band of the QDs.[32] Incorporation of the QDs is also expected to enhance the photon absorption in the visible (vis) region of the solar spectrum and harvest a larger spectral span of the vis light, which otherwise cannot be sufficiently absorbed by TiO_2. Hence, a major enhancement in the photocatalytic $DeNO_x$ performance of TiO_2 is anticipated upon the proposed QD incorporation. Photocatalytic activity of different composite materials was reported to be greatly enhanced with the incorporation of CdTe QDs.[33,34]

Along these lines, we synthesized thioglycolic acid (TGA)-capped CdTe QDs for the surface functionalization of TiO_2. Commercially available Degussa P25 (produced by Evonik, purchased from Sigma-Aldrich) was employed as both the benchmark TiO_2 photocatalyst and the support material for the QDs. P25 is a well-known photocatalyst, which has been thoroughly utilized and characterized in a vast number of former studies,[35−39] including some of our former works.[5−8] Direct comparison of raw/absolute photocatalytic activities of different catalysts tested under different experimental conditions, reactors, and illumination conditions may lead to misleading conclusions. Thus, use of a benchmark catalyst and reporting photocatalytic performance results relative to a commonly used benchmark catalyst (P25) eliminates many inconsistencies due to variations in the experimental conditions.

P25 typically contains 78−85 wt % anatase, 14−17 wt % rutile, and 0−13 wt % amorphous titania phases. Specific surface area (SSA) of P25 was reported to range within 35−65 m^2/g, where the currently used P25 material had an SSA of 50 m^2/g. Characteristic particle size, pore volume, and pore diameter of P25 were measured to be within 20−30 nm, 0.18−0.25 cm^3/g, and 7−18 nm, respectively.[35−39] The copresence of crystalline anatase and rutile domains in P25 and the heterojunctions at their interfaces were reported to create a synergetic effect enhancing photocatalytic activity.[40,41] It was claimed that photogenerated electrons of the rutile phase can migrate to the conduction band of the anatase phase, which could increase the lifetime of the photogenerated excitons and decrease the recombination rate.[42−44] On the other hand, such a synergetic effect was not observable when separate anatase and rutile phases were physically mixed together.[45]

Due to its large band gap (3.0−3.2 eV) and high electron−hole recombination rate,[22] P25 needs to be structurally enhanced to enhance its photocatalytic NO_x storage performance in both UV and vis spectral regions. Therefore, in this study, a significant performance enhancement was achieved by incorporating CdTe QDs on P25. Thioglycolic acid ($HSCH_2COOH$)-capped CdTe QDs were chosen owing to their suitable band gap (1.96 eV) enabling vis light absorption. CdTe QDs on P25 were expected to improve vis light harvesting and decrease the electron−hole recombination rate. Furthermore, utilized CdTe QDs were conveniently suspended in an aqueous medium rather than an organic solvent. With the volatile organic liquid-phase dispersants, sustaining the stability of the colloidal suspension for extended durations of time could be challenging due to the loss of the liquid medium via evaporation. Moreover, organic molecules used in the dispersant medium can readily functionalize P25 surface in an uncontrolled and complex manner and change its photocatalytic properties. These unwanted/uncontrolled surface functionalities can also lead to unwanted surface transformations/poisoning particularly under UV or vis irradiation or upon exposing the photocatalyst to reaction conditions.

2. EXPERIMENTAL SECTION

2.1. Synthesis of CdTe QDs. The protocol for the colloidal synthesis of TGA-capped CdTe QDs dispersed in water was adopted from the work of Rogach et al.[46] First, 4.59 g of the Cd precursor (cadmium perchlorate hexahydrate, $Cd(ClO_4)_2{\cdot}6H_2O$, Alfa Aesar) was dissolved in 250 mL of Milli-Q water in a 1 L three-neck flask. The reaction system was constantly stirred with a magnetic stirrer throughout the synthesis protocol. Milli-Q water (250 mL) and thioglycolic acid (TGA, 1 mL, 1.33 g; Sigma-Aldrich, 98%) were injected simultaneously into the reaction flask. TGA was used as the capping agent of the QDs. While the flask was stirred, 1 M sodium hydroxide solution (NaOH(aq)) was prepared aside. This NaOH(aq) solution was used to adjust the pH of the reaction system to ca. 11.8−12.0. Next, 0.8 g of the Te precursor (aluminum telluride (Al_2Te_3), Cerac Inc.) was placed into a 25 mL three-neck flask. As aluminum telluride is extremely sensitive to oxygen, Ar(g) was used to sweep off the oxygen from the reaction system. Since harmful hydrogen telluride (H_2Te) gas was released from the system in the next steps, an absorption flask containing 10% NaOH(aq) solution was connected to the system to capture $H_2Te(g)$ before escaping into the air. Then, 0.5 M sulfuric acid ($H_2SO_4(aq)$) was injected using a syringe into the three-neck flask containing aluminum tellurite in a dropwise fashion. $H_2Te(g)$ was released through the chemical reaction given in eq 1

$$Al_2Te_3(aq) + 3H_2SO_4(aq) \rightarrow 3H_2Te(g) + Al_2(SO_4)_3(aq) \quad (1)$$

$H_2Te(g)$ was passed through the reaction flask with Ar(g) flow for half an hour until the color of the solution turned pink. Then, the 25 mL three-neck flask was detached from the system and the reaction flask was heated at 100 °C, while condensing the evaporated water vapor back into the reaction flask with the help of a chiller. QD growth commenced with the boiling of the reaction suspension. By altering the boiling time, the size of the QDs and the optical properties can be tuned. After the 1st min of the boiling, emission spectrum of the obtained QDs appeared blue. Within 5−10 min of boiling, emission shifted to green and eventually to red. After deciding on the emission wavelength, therefore the boiling time, the reaction was stopped by cooling the reaction medium. Once the system was cooled down, QDs were filtered and cleaned by centrifuging with Milli-Q water at 4500 rpm for 5 min and they were stored in aqueous medium in the dark at room temperature. For this particular work, the

DOI: 10.1021/acsami.8b18036
ACS Appl. Mater. Interfaces 2019, 11, 865−879

molar concentration of the QD suspension was increased 3 times. For 15 mL of QD aqueous suspension, 7.5 mL of isopropanol was added to precipitate the dots. After centrifuging and drying, the precipitated dots were added to 5 mL of Milli-Q water.

2.2. Synthesis of CdTe/P25 and CdTe/Al_2O_3 Composite Materials. For the preparation of CdTe(aq)/TiO_2 composite materials, different volumes of the CdTe aqueous suspension with a CdTe QD concentration of ca. 5.4×10^{-5} M were drop-cast on 250 mg of P25 TiO_2 powder in a 6 cm diameter Petri dish. After physically mixing for 2 min, the slurry was placed in an oven and dried at 70 °C for 18 h (see Figure S2 in the Supporting Information). To rule out any major influence of aqueous dispersant on photocatalytic activity measurements, control experiments were performed, where pure H_2O(l) was dosed on P25 with volumes that were identical to the ones used in QD functionalization. Since the capping agent (i.e., TGA) can also play a part in the photocatalytic DeNO$_x$ process, additional control experiments were carried out, where TGA(aq) was dosed on P25. The aqueous solution of TGA was prepared according to the initial concentration of TGA in the colloidal synthesis of the QDs. For this reason, 1 mL (1.33 g) of TGA was dispersed in 250 mL of deionized water. The solution was sonicated for 30 min. The same steps were followed for the H_2O(l)/TiO_2 and the TGA(aq)/TiO_2 control samples. Further control experiments using CdTe/P25 without TGA capping were not performed, as removal of TGA capping may lead to structural modifications in the CdTe system, agglomeration of QDs, and deposition of TGA or other organic residues on titania. For additional control experiments without titania, CdTe/Al_2O_3, TGA(aq)/Al_2O_3, and H_2O(l)/Al_2O_3 materials were also prepared in an identical fashion with respect to their titania analogues, where SASOL Puralox SBA200 γ-Al_2O_3 was used as the (nonphotocatalytic) support material. Acronyms of the prepared samples and the amounts of the chemicals used in their preparations are listed in Table S1.

2.3. Characterization. X-ray diffraction (XRD) patterns of the samples were obtained by using a Panalytical Multi-Purpose X-ray diffractometer equipped with a Cu Kα (1.5405 Å) X-ray source operating at 45 kV/40 mA. Transmission electron microscopy (TEM), high-angle annular dark-field scanning transmission electron microscopy (HAADF-STEM), and energy-dispersive X-ray analysis (EDX) measurements were carried out using an FEI Tecnai G2F30 transmission electron microscope. A Cary 100 UV−vis spectrometer was used for acquiring UV−vis absorption spectra. Diffuse reflectance UV−vis (DR-UV−vis) spectra were obtained using a Cary 5000 UV−vis−NIR spectrometer equipped with a Varian Cary 2500 DR accessory. Photoluminescence (PL) of the QDs was measured by using a Cary Eclipse Fluorescence Spectrophotometer. The absolute photoluminescence quantum yield (PL-QY) of CdTe QDs was measured by using integrating sphere with the help of Ocean Maya2000 Spectrometer. Time-resolved fluorescence measurements were conducted using a PicoQuant FluoTime 200 Spectrometer equipped with a picosecond pulsed laser excitation source (375 nm), and the fluorescence decay curves were recorded with TimeHarp time-correlated single-photon counting unit. The Brunauer−Emmett−Teller (BET) specific surface area (S_{BET}, m^2/g) measurements were carried out by low-temperature isothermal adsorption−desorption of N_2 using a Micromeritics TriStar 3000 apparatus. X-ray photoelectron spectroscopy (XPS) measurements were performed using a Thermo Fisher K-Alpha X-ray photoelectron spectrometer with monochromatized X-rays of 1486.6 eV.

2.4. Photocatalytic NO$_x$ Oxidation and Storage Measurements. Photocatalytic NO$_x$ oxidation and storage performance measurements were conducted using a custom-design photocatalytic flow reactor system shown in Figure S1, which was designed considering the ISO 22197-1:2007 standard.[47−49] Inlet gas mixture that was introduced to the reactor contained 0.750 standard liters per minute (SLM) N_2(g) (purity: 99.99%, Linde GmbH), 0.250 SLM O_2 (purity: 99%, Linde GmbH), and 0.010 SLM NO (100 ppm NO(g) diluted in balance N_2(g), Linde GmbH). To obtain the gas flow values given above, mass flow controllers (MKS1479A for N_2(g) and O_2(g) and Teledyne HFC-202 for NO(g) diluted in N_2(g)) were utilized so that the total gas flow over the photocatalyst was kept at 1.010 SLM, where the NO(g) content of the inlet gas mixture was fixed at 1 ppm. The pressure inside the reactor was kept at ca. 1 bar and measured via a MKS Baratron 622B capacitance manometer. Humidity of the inlet gas mixture was also carefully controlled by dosing varying amounts of water vapor into the inlet gas mixture (i.e., before the reactor entrance; see Figure S1) with the help of a PermSelect (PDMSXA-2500) semipermeable membrane module attached to an external variable-temperature water chiller/recycler. Typical relative humidity of the reactor was kept within 50 ± 3% at 23 ± 2 °C, measured at the sample position using a Hanna HI 9565 humidity analyzer. Changes in the NO, NO_2, and total NO$_x$ gas concentrations at the outlet of the reactor were monitored using a chemiluminescent NO$_x$ analyzer, Horiba Apna-370 (Figure 1) with a sensitivity level of 0.1 ppb.

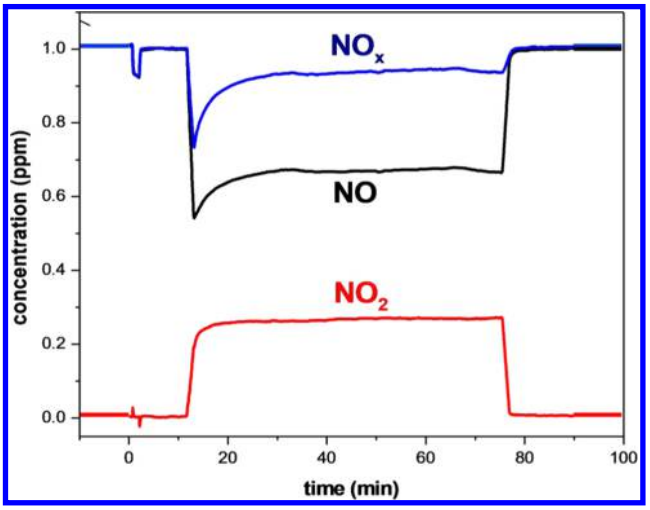

Figure 1. Representative concentration vs time plot for a photocatalytic NO$_x$ oxidation and storage experiment measured via chemiluminescence NO$_x$ analyzer located at the outlet of the reactor, where the bottom (red) profile shows NO_2(g) concentration, the middle (black) profile shows NO(g) concentration, and the top profile (blue) shows total NO$_x$(g) concentration defined by the summation of NO(g) and NO_2(g) concentrations, all as a function of time.

For the experiments performed with UV-A irradiation, an 8 W UV-A lamp (F8W/T5/BL350, Sylvania, Germany) was used, while for the experiments carried out with vis light illumination, a 35 W metal halide lamp (HCI-TC 35 W/942 NDL PB 400−700 nm range, Osram) was utilized. Since the currently used vis light source also emitted a limited but detectable flux of UV light, a commercial vis-transparent UV-blocker/filtering film (LLumar window film UV CL SR PS (clear)) was placed on top of the reactor during the vis light experiments. This was crucial for ruling out any contribution from UV photons during the vis light illumination. The incoming light flux was measured carefully before and after each UV-A and vis light measurements separately with a photoradiometer (HD2302.0, Delta Ohm/Italy) using a UV-A probe (315−400 nm) and a PAR vis probe (400−700 nm), respectively. Typical vis light photon flux used in the current experiments was within 450−500 μmol/(m^2 s), while typical UV-A-light power density was 7.7−8.3 W/m^2. Note that the photon flux of the vis light source was about 15 times greater than that of the UV-A light source. Relative percentile of vis photon flux in typical solar radiation is also significantly greater than that of UV-A photon flux (i.e., 42% vis vs 6% UV-A). Reactor temperature remained within 23 ± 2 °C during UV-A measurements, whereas during vis light experiments, reactor temperature reached up to 42°C after a typical 60 min photocatalytic activity test.

For each photocatalytic performance measurement, 200 mg of the photocatalyst was pressed into a 0.5 mm deep 40 × 40 mm

DOI: 10.1021/acsami.8b18036
ACS Appl. Mater. Interfaces 2019, 11, 865−879

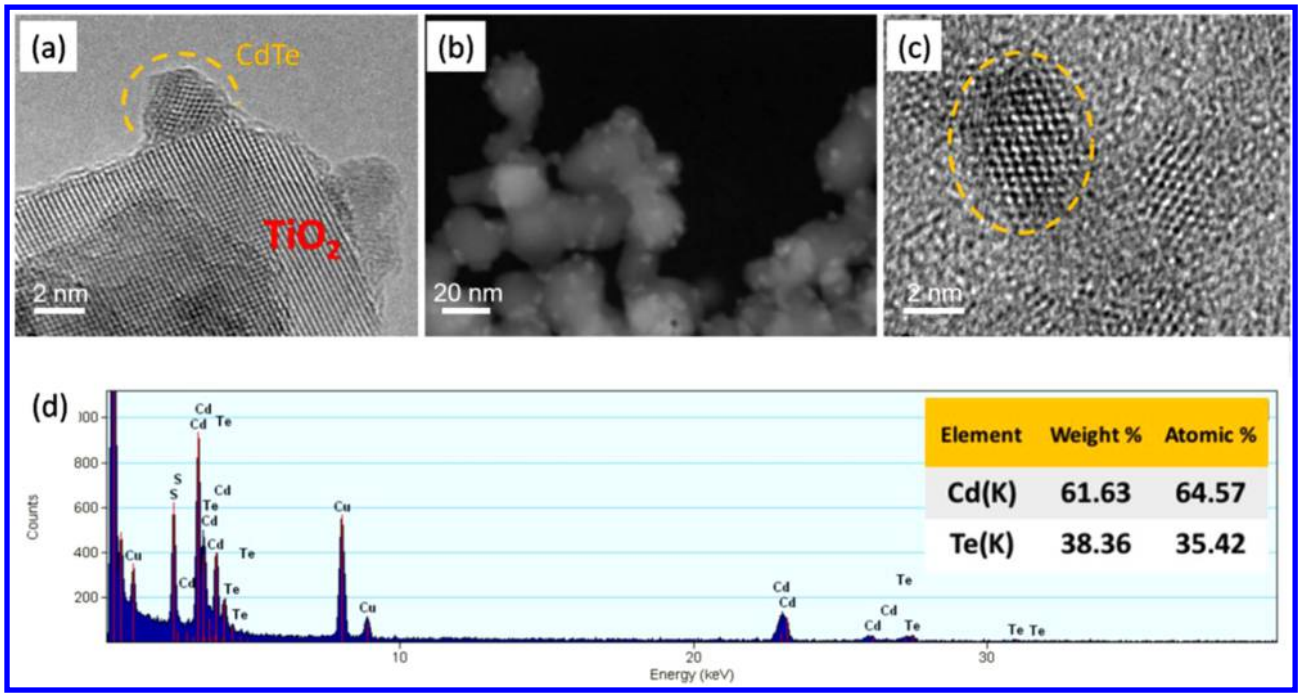

Figure 2. (a) Bright-field TEM image of CdTe/P25 composite material. (b) HAADF-STEM image of CdTe/P25. (c) TEM image of CdTe quantum dots without TiO_2. (d) EDX spectrum of the CdTe quantum dots.

poly(methyl methacrylate) (PMMA) sample holder. Figure 1 shows a typical concentration versus time curve for a photocatalytic activity test. In this experiment, an inlet gas mixture containing 1 ppm NO(g) was initially fed to by-pass line of the reactor in dark (t < 0 min).

At t = 0 min, gas mixture was introduced into the reactor in the dark, leading to a transient decrease in NO(g) due to the expansion of the gas into the reactor and adsorption on the reactor walls and catalyst surface (Figure 1). Note that there was no photocatalytic action at this time as irradiation source was still turned off. Hence, the decrease in NO(g) concentration was minuscule and also temporary. At ca. t = 12 min, irradiation light source was turned on, resulting in drastic and longer-term changes in NO(g) and NO_2(g) concentrations due to the photocatalytic action, where increase in NO_2(g) level was caused by NO(g) oxidation and decrease in NO(g) level was due to both NO_2(g) generation and solid state NO_x storage (PHONOS) on the photocatalyst surface.

3. RESULTS AND DISCUSSION

3.1. Characterization of As-Prepared Catalysts. Figure 2a shows the bright-field high-resolution TEM image of the CdTe/TiO_2 composite system revealing CdTe QDs dispersed on P25 (titania) support material. HAADF-STEM image given in Figure 2b reveals that CdTe QDs have an average particle size of 3.5−4.0 nm. High-resolution TEM image of the QDs directly obtained from the aqueous suspension without P25 (Figure 2c) suggests that QD average particle size remained almost constant after their incorporation on the P25 surface due to the TGA-capping on CdTe, preventing agglomeration. EDX data corresponding to QDs directly obtained from the aqueous suspension without P25 presented in Figure 2d clearly verifies the presence of Cd and Te. QDs were found to be composed of 62 wt % Cd and 38 wt % Te with an atomic composition of $Cd_{0.65}Te_{0.35}$. Note that the S signal in the EDX spectrum in Figure 2d originates from the TGA capping agent and Cu signal is associated with the TEM sample holder grid.

Crystal structures of the CdTe QDs, P25, and CdTe/P25 composites were investigated by XRD (Figure 3). XRD profile for CdTe QDs without TiO_2 (Figure 3a) reveals diffraction

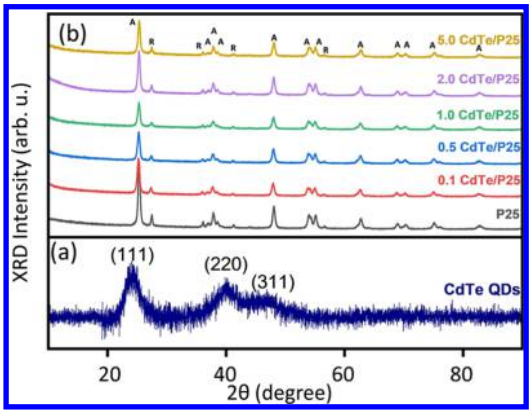

Figure 3. XRD patterns of (a) CdTe QDs without TiO_2 and (b) P25 and CdTe/P25 composite materials with increasing CdTe QD loadings. A: anatase (ICDD card no.: 00-021-1272), R: rutile (ICDD card no.: 00-021-1276).

signals at 23.7, 39.8, and 46.5°, which can readily be assigned to (111), (220), and (311) facets of CdTe nanoparticles having zinc-blende structure, respectively.[46] As can be expected from small nanoparticles with an average particle size in the range of 3−4 nm, XRD signals for QDs are fairly broad (Figure 3a).[50] XRD profile of P25 presented in Figure 3b exhibits characteristic diffraction signals indicating the presence of typical anatase and rutile domains. Diffraction patterns of the QD-functionalized CdTe/P25 composites have identical XRD profiles to P25, for all of the CdTe loadings used in the current work. This is consistent with the small loadings and small particle sizes of the CdTe QDs utilized for the functionalization of P25, which do not lead to any discernible diffraction signals in XRD pattern. The use of minuscule loadings of CdTe is advantageous in terms of minimizing material cost and toxicity.[51,52]

DOI: 10.1021/acsami.8b18036
ACS Appl. Mater. Interfaces 2019, 11, 865−879

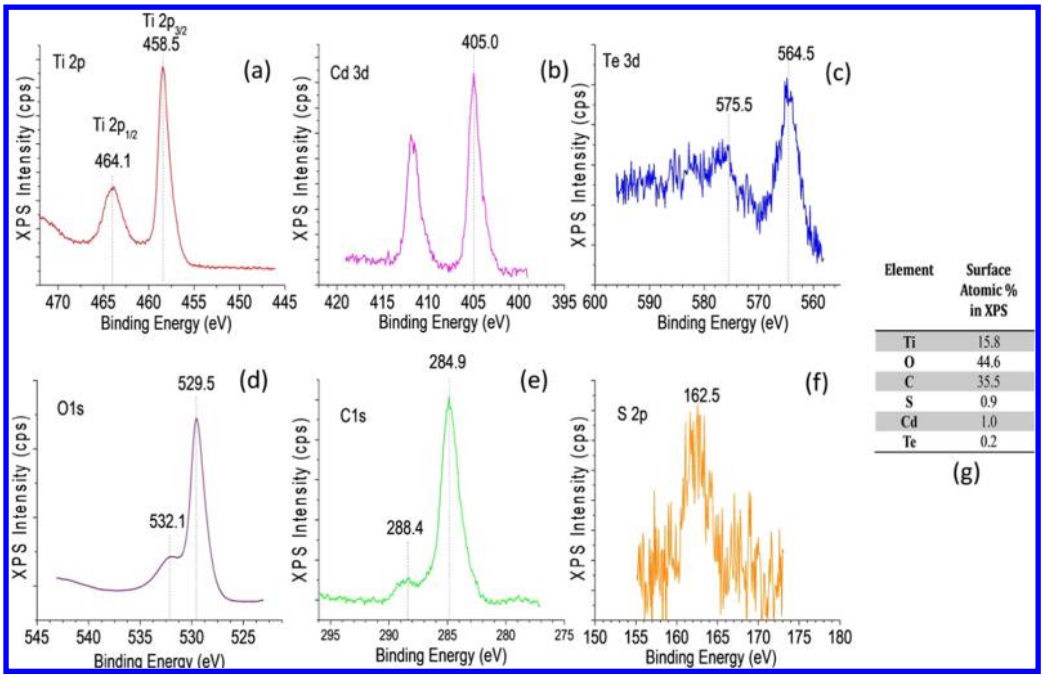

Figure 4. XPS analyses of the CdTe/P25 composite material: (a) Ti 2p, (b) Cd 3d, (c) Te 3d, (d) O 1s, (e) C 1s, (f) S 2p regions, and (g) surface atom % values obtained via integrated XPS peak areas that were normalized using the corresponding photoemission cross sections.

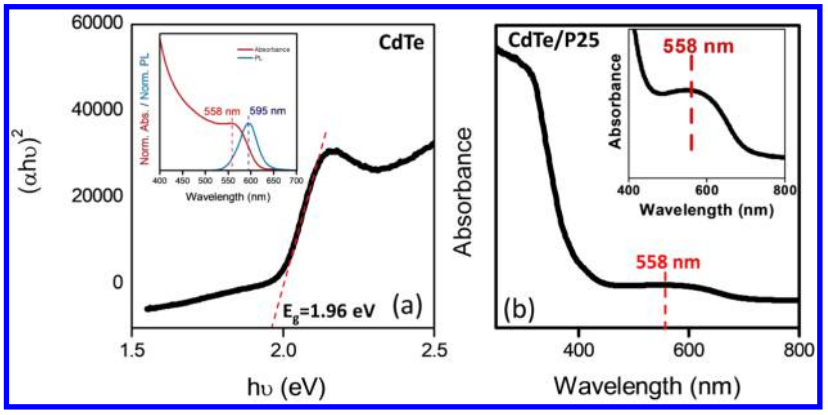

Figure 5. (a) Tauc plot for pure CdTe QDs (i.e., without P25) obtained from DR-UV−vis spectrum (inset shows the corresponding UV−vis absorbance and photoluminescence (PL) spectra), (b) UV−vis absorbance spectra of CdTe/TiO_2 composite material (inset shows the detailed view of the shoulder due to CdTe absorption edge).

Figure 4 presents the XPS analysis results of the CdTe/P25 composite system. In Figure 4a, Ti $2p_{1/2}$ and Ti $2p_{3/2}$ features of P25 (TiO_2) can be observed at 464.1 and 458.5 eV, respectively. These binding energy values are about 0.6 eV lower than the typical values of P25 (data not shown), indicating an active electronic interaction between CdTe QDs and the titania support in the CdTe/P25 composite system in very good accordance with similar observations on carbon quantum dot (CQD)-functionalized P25 systems (i.e., CQD/P25).[52] The presence of a Cd $3d_{5/2}$ feature at 405.0 eV in Figure 4b suggests the existence of predominantly CdTe species and the lack of significant amounts of CdO_x. The Te $3d_{5/2}$ feature located at 575.5 eV in Figure 4c is slightly higher than the Te $3d_{5/2}$ states expected in CdTe.[53] Thus, in addition to CdTe species, the presence of additional TeO_x species cannot be ruled out. The O 1s feature at 529.5 eV in Figure 4d corresponds to the oxygen species in the P25 structure, whereas the O 1s feature at 532.1 eV can be attributed to oxygen species linked to C atoms in the TGA capping agent.[54] C 1s signal at 284.9 eV in Figure 4e can be ascribed to surface (adventitious) carbon on P25, whereas the C 1s shoulder at 288.4 eV can be associated with C species in the TGA capping agent. The presence of sulfur is also evident by the weak S 2p signal located at 162.5 eV in Figure 4f. Surface atomic compositions were also determined using the XPS data, as shown in Figure 4g. It is apparent that surface of the CdTe/P25 system contained a large amount of carbon (35.5 atom %) mostly due to adventitious C on P25 with a smaller contribution due to C species associated with the TGA capping agent. The presence of a significant amount of adventitious C on pure P25 (i.e., without CdTe QDs) was also observed in our former XPS measurements on pure P25 (data not shown) and most likely originated from the organic ligands of the Ti precursors used in TiO_2 synthesis that were not entirely removed from the surface after calcination. Surface of the CdTe/P25 system also revealed 44.6 atom % oxygen and 0.9 atom % sulfur, where the latter exclusively originated from the TGA capping agent. XPS analysis also indicated the

DOI: 10.1021/acsami.8b18036
ACS Appl. Mater. Interfaces 2019, 11, 865−879

presence of 1.0 atom % Cd and 0.2 atom % Te on the CdTe/P25 surface, which was consistent with the small CdTe loadings used in the current work. Differences between the relative Cd and Te elemental composition values obtained by TEM-EDX (Figure 2d) as opposed to XPS (Figure 4g) can be explained by considering the fact that TEM-EDX measurements are local in nature. In other words, TEM-EDX measurements involve a spot size (beam size), which is only a few nanometers in diameter. On the other hand, during the XPS measurements, a much larger spot size is irradiated by X-rays with a diameter in the millimeter range. However, both of the current TEM-EDX and XPS experiments unequivocally verify the presence of Cd and Te in the CdTe QD system, where Cd exists in a relatively excess amount.

The Kubelka–Munk function, $F(R)$ given in eq 2,[55] allows the estimation of the optical absorption of a sample from its reflectance (R)

$$F(R) = \frac{(1 - R)^2}{2R} \tag{2}$$

Accordingly, the calculation of direct or indirect band gaps can be done according to Tauc expression (eq 3)[56]

$$(h\nu\alpha)^n = A(h\nu - E_g) \tag{3}$$

where E_g is the band gap, h is Planck's constant, ν represents the photon frequency, α is the absorption coefficient, and A is the proportionality constant. For direct band gap materials, n = 2, whereas for indirect materials, n = 0.5. Since CdTe is a direct band gap semiconductor, n was taken as 2.

Figure 5a presents the Tauc plot for the CdTe QDs (without P25) revealing a direct band gap of 1.96 eV (632 nm). As expected, this is higher than the band gap of bulk CdTe (1.44 eV)[57] due to quantum size/confinement effect.[58,59]

The inset in Figure 5a shows that CdTe QDs have an absorption shoulder at 558 nm and exhibit a photoluminescence spectrum with an emission maximum at 595 nm. Thus, it is apparent that CdTe QDs can harvest both UV and vis light. Figure 5b shows the UV–vis absorption spectrum of CdTe/P25 composite material. CdTe/P25 also features the characteristic absorption shoulder for CdTe QDs with a maximum at 558 nm and an additional edge for the adsorption of P25 starting at ca. 400 nm (i.e., 3.09 eV) consistent with the band gaps of the rutile (3.0 eV) and anatase (3.2 eV) phases in P25.[22]

The average size of the CdTe quantum dots can be estimated using the data in Figure 5 and the empiric relation given in eq 4,[60] where D is the average diameter of CdTe particles and λ is the wavelength of first excitonic absorption peak (i.e., 558 nm).

$$D = (9.8127 \times 10^{-7})\lambda^3 - (1.7147 \times 10^{-3})\lambda^2 + (1.0064)\lambda - (194.84) \tag{4}$$

Accordingly, the average diameter of the CdTe QDs was estimated to be 3.3 nm, which is in perfect agreement with the current TEM data (Figure 2). One can also estimate the extinction coefficient of the CdTe QDs using eq 5,[60] where ΔE is the transition energy (i.e., 2.22 eV) corresponding to the first absorption peak at 558 nm.

$$\varepsilon = 3450\Delta E(D)^{2.4} \tag{5}$$

Hence, the extinction coefficient of CdTe QDs can be found as 1.55×10^5 cm^{-1} M^{-1}. This information can also be exploited to determine the effective concentration of CdTe QDs in the prepared aqueous suspensions for photocatalyst synthesis. To this end, we resort to the Beer–Lambert law given in eq 6, where A is the absorbance at the first excitonic peak (i.e., 0.269), ε is the extinction coefficient (1.55×10^5 cm^{-1} M^{-1}), c is the concentration, and b is the path length (i.e., 1 cm)

$$A = \varepsilon bc \tag{6}$$

Thus, for a 100 μL CdTe QD suspension diluted in 3 mL of water, CdTe concentration can be found as ca. 1.74×10^{-6} M, while the QD suspension used in the preparation of CdTe/P25 photocatalysts can be estimated to be ca. 5.4×10^{-5} M.

To further understand the emission properties of our QD samples, we measured its PL quantum yield (PL-QY) and fluorescence lifetime in solution. The PL-QY of the QDs was found to be 40%, which is in a good agreement with the literature.[46] Moreover, the time-resolved PL decay of CdTe QDs in the absence of P25 is depicted in Figure 6. The decay curve was fitted with three-exponential functions, and the amplitude-averaged fluorescence lifetime of the sample was found to be ca. 20.6 ns.

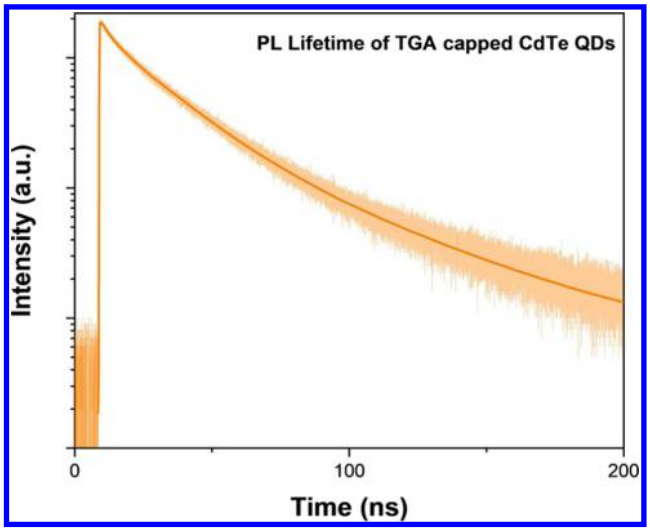

Figure 6. Time-resolved photoluminescence (PL) decay of CdTe quantum dots (without P25).

3.2. Photocatalytic Removal of NO(g). Photocatalytic activity measurements were conducted using either UV-A or vis light (Figure 7) irradiation sources over fresh or aged CdTe/P25 catalysts with varying CdTe loadings. Aged catalysts were prepared by exposing the catalysts to UV-A or vis light source under ambient conditions for 18 h prior to the photocatalytic activity measurements. Furthermore, additional photocatalytic activity measurements were also carried out with control samples, including pure P25, TGA(aq)/P25, H_2O(l)/P25, alumina, CdTe/alumina, TGA(aq)/alumina, and H_2O(l)/alumina.

3.2.1. Photocatalytic Performance of P25 Titanium Dioxide Benchmark Photocatalyst. PHONOS performance of pure P25 in fresh and aged forms was investigated under UV-A and vis illumination, and the results are presented in Figure 7a,b along with their corresponding DeNO$_x$ index values (Figure 8a,b), respectively. It is apparent that both fresh and aged P25 had moderate-to-high NO conversion (31% in

DOI: 10.1021/acsami.8b18036
ACS Appl. Mater. Interfaces 2019, 11, 865–879

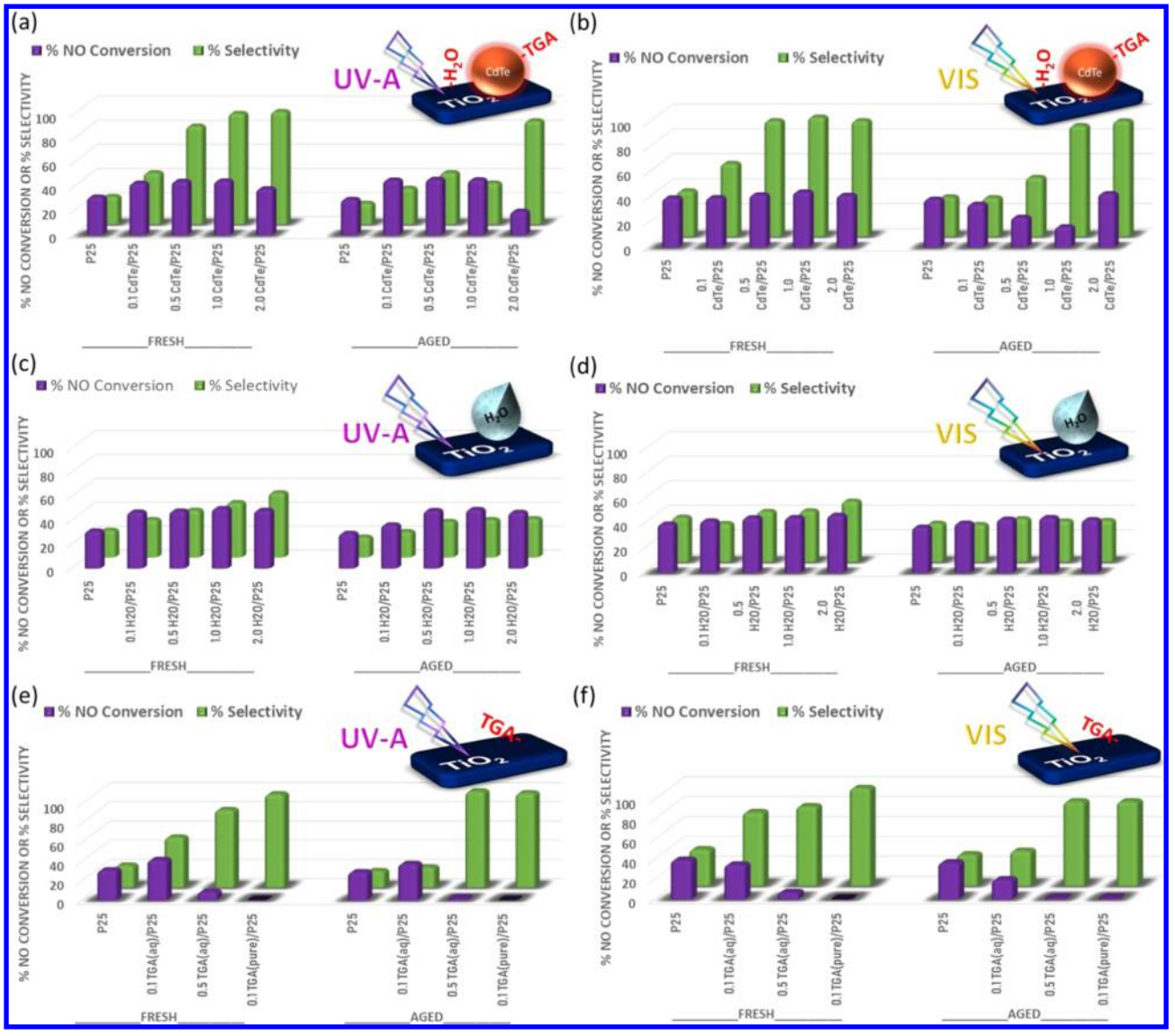

Figure 7. NO conversion and selectivity results for fresh and aged titanium dioxide (P25) and CdTe/P25 under (a) UV-A irradiation and (b) vis irradiation; $H_2O(l)$/P25 under (c) UV-A irradiation and (d) vis irradiation; and TGA(aq)/P25 and TGA (pure)/P25 under (e) UV-A irradiation and (f) vis irradiation.

UV-A and 40% in vis) and relatively low selectivity (25% in UV-A and 35% in vis). Aging did not lead to very significant changes in PHONOS performance of P25. Conversion and selectivity of P25 were found to be higher in the vis light experiments. However, this does not mean that P25 was more active under vis light, since the photon flux used in the vis experiments was about 15 times greater than that of UV-A experiments. This is also evident in the corresponding % photonic efficiency results presented in Figure S3, suggesting significantly lower % NO_x storage photonic efficiency for P25 under vis illumination compared to UV-A. On the other hand, it is important to emphasize that under currently used vis photon flux values, P25 had a considerable photocatalytic activity. Nevertheless, under all of the currently investigated conditions, pure P25 titania had significantly negative $DeNO_x$ index values (Figure 8a,b), suggesting that in $NO(g) + O_2(g)$ reaction, P25 tends to increase the toxicity of the gas mixture rather than providing photocatalytic NO_x abatement. In other words, P25 can efficiently photooxidize $NO(g) + O_2(g)$ into NO_2; however, it fails to store photogenerated NO_2. Instead, it releases toxic $NO_2(g)$ to the atmosphere in perfect agreement with previous studies.[9,61]

3.2.2. Photocatalytic Performance of Fresh CdTe/P25 Composite Photocatalysts. Incorporation of fresh CdTe QDs on P25 was found to result in a minor increase in NO conversion both under UV-A and vis irradiation as opposed to pure P25, where the increase in NO conversion was particularly more pronounced in UV-A case (Figure 7a,b). For the fresh 1.0 CdTe/P25 catalyst, NO conversion reached 42 and 43%, while selectivity reached 92 and 97% under UV-A and vis illumination, respectively. For the fresh CdTe/P25 catalysts with different QD loadings, a volcano behavior in PHONOS performance was visible, in terms of both NO conversion and selectivity values (Figure 7a,b) as well as in terms of $DeNO_x$ index values (Figure 8a,b). It was observed that fresh 1.0 CdTe/P25 and 2.0 CdTe/P25 samples delivered the best photocatalytic NO_x abatement performances with the most positive $DeNO_x$ index values under both UV-A and vis illumination conditions. Fresh 1.0 and 2.0 CdTe/P25 photocatalysts were able to store significant amounts of NO_x in the

DOI: 10.1021/acsami.8b18036
ACS Appl. Mater. Interfaces 2019, 11, 865−879

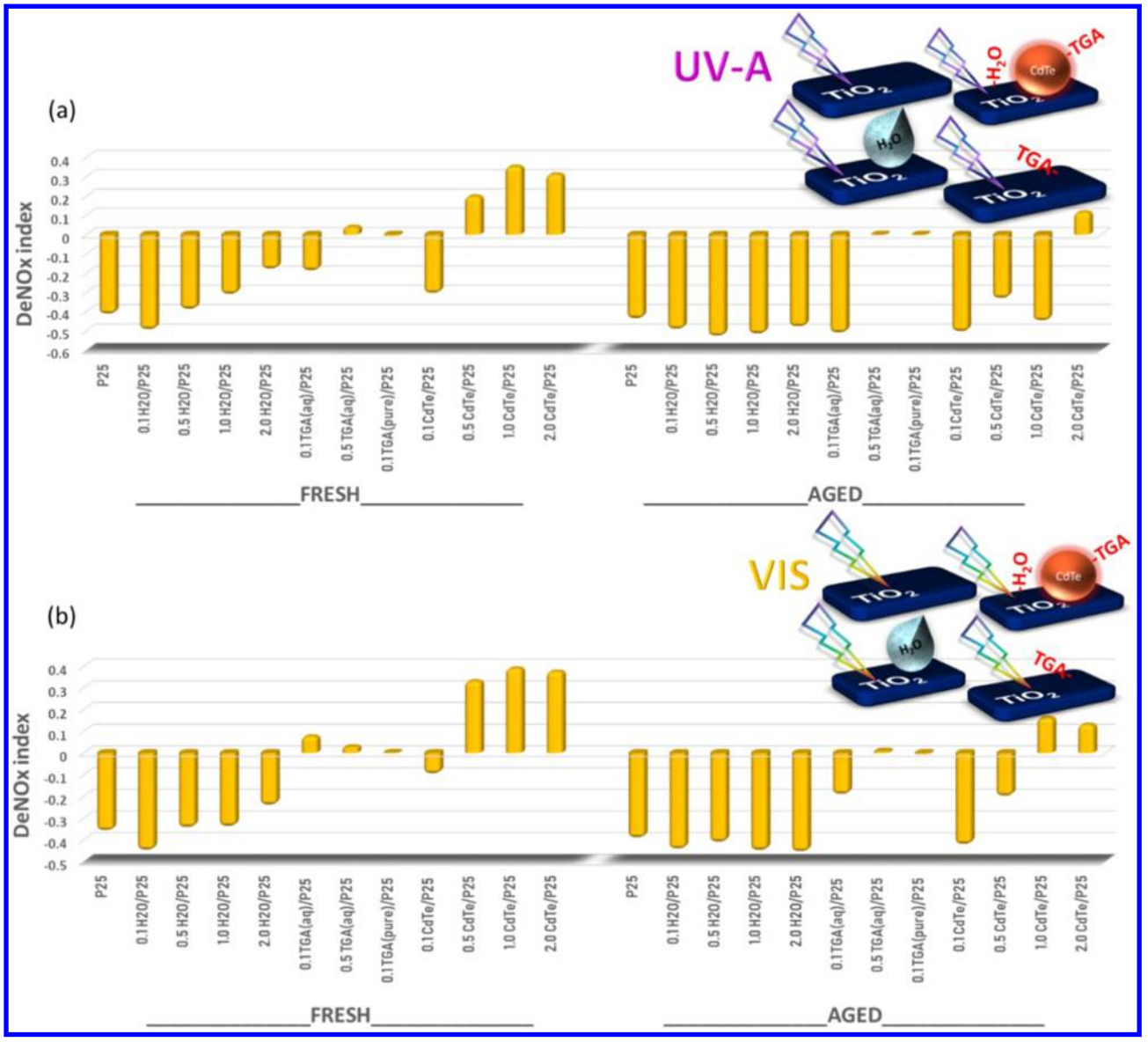

Figure 8. DeNO$_x$ index results of fresh and aged titanium dioxide (P25), CdTe/P25, H$_2$O(l)/P25, TGA(aq)/P25, and TGA (pure)/P25 under (a) UV-A and (b) vis irradiation.

solid state, while suppressing $NO_2(g)$ release almost completely both under UV-A and vis irradiation. In other words, fresh 1.0 and 2.0 CdTe/P25 photocatalysts were capable of efficiently harvesting solar radiation in a quite broad spectral window starting from UV-A and extending toward vis region. Thus, it is clear that incorporation of CdTe quantum dots to titania changed the negative DeNO$_x$ index of pure titania P25 (−0.42 in UV-A and −0.35 in vis) to significantly positive values (+0.35 in UV-A and +0.40 in vis), rendering the fresh CdTe/P25 system an efficient broad-band photocatalyst with a strong NO_x abatement effect. Figures 7a and 8a reveal that very high loadings of CdTe (e.g., fresh 2.0 CdTe/P25) led to a minor but detectable attenuation of NO conversion and selectivity under UV-A irradiation. This was probably due to the blocking/quenching of the photocatalytic active sites of titania (that can harvest UV-A photons) or substitution of the surface −OH functionalities of titania with TGA capped-QDs at high QD surface coverages. In contrast, under vis irradiation (Figures 7b and 8b), fresh and aged 2.0 CdTe/P25 can still exhibit relatively good performance. This may suggest that both QDs and titania sites are associated with the vis-active sites of the catalytic system.

Photocatalytic performance trends discussed above suggest that the primary photocatalytic active sites of the CdTe/P25 system that are responsible for the $NO(g) + O_2(g)$ photooxidation process reside on titania, since addition of TGA-capped CdTe QDs led to only a minor boost in NO conversion. However, a synergistic effect between CdTe QDs and titania (moderately increasing the NO conversion capability) cannot be ruled out, particularly under UV-A irradiation. On the other hand, while QDs seem to increase NO conversion to a certain extent, the more noteworthy function of TGA-capped CdTe QDs is probably the photocatalytic conversion and storage of photogenerated NO_2 species into other oxidized surface species, such as HONO, $HONO_2$, NO_2^-, NO_3^-, and −S−R−NO_x (i.e., NO_x bound to TGA). It is well known that $NO(g) + O_2(g)$ mixtures as well as $NO_2(g)$ can readily adsorb on numerous metal oxide surfaces in the form of nitrates, nitrites, as well as their protonated acidic forms.[62−68] NO_x adsorption and successive

DOI: 10.1021/acsami.8b18036
ACS Appl. Mater. Interfaces 2019, 11, 865−879

oxidation and storage in the form of nitrates also serve as the basis of the nonphotocatalytic technology called NO_x storage reduction, which is also called lean NO_x traps that is commonly used in tail-pipe emission control systems of automobiles. As will be demonstrated below via further control experiments with TGA(aq)/TiO_2, NO_2 capture cannot be solely achieved by the TGA capping (without CdTe QDs) through a simple adsorption process, but rather involves a photocatalytic action triggered by the entire TGA-CdTe QD system.

3.2.3. Photocatalytic Performance of Aged CdTe/P25 Composite Photocatalysts. Aging of the CdTe/P25 photocatalysts under UV-A or vis irradiation for 18 h under ambient conditions led to interesting alterations in the photocatalytic performance trends (Figures 7 and 8). In the case of UV-A irradiation (Figures 7a and 8a), NO conversion was not notably affected by aging up to a QD loading of 2.0 mL, while selectivity severely decreased. In other words, while aged CdTe/P25 catalysts were still able to carry out NO(g) + O_2(g) photooxidation process efficiently, they failed to store the generated NO_2 species on the catalyst surface. Instead, they released NO_2(g) to the atmosphere, decreasing selectivity. We believe that this could be due to degradation of the organic TGA capping on the CdTe QD and/or oxidation of the QD system. Under UV-A illumination, for the aged CdTe/P25 catalysts with 0.1, 0.5, and 1.0 mL QD loadings (Figure 7a), NO conversion seemed to be unaffected by the aging process, suggesting that most of the photocatalytic active sites on titania domains could still function. However, low selectivity within this QD loading region indicates that TGA-capped CdTe system undergoes unfavorable transformations upon extended illumination under UV-A. An interesting behavior was also observed for the UV-A aged 2.0 CdTe/P25 sample. For this catalyst, active sites of titania responsible for the NO(g) + O_2(g) photooxidation were partially poisoned/inhibited by the UV-A aging process, decreasing the NO(g) + O_2(g) photooxidation rate along with the NO_2(g) generation rate. Thus, this relatively smaller amount of NO_2(g) can readily/effectively be stored on the UV-A aged 2.0 CdTe/P25 surface, leading to a high selectivity at the expense of diminished NO conversion. Accordingly, this particular catalyst showed a small but positive $DeNO_x$ index, unlike all of the other UV-A aged CdTe/P25 samples.

Similar aging characteristics at least to a certain extent were also observed for the vis light experiments (Figure 7b). In other words, for the vis-aged CdTe/P25 catalysts with 0.1, 0.5, and 1.0 mL QD loadings, poisoning of titania due to degradation of the TGA-capped CdTe QDs led to decreased NO conversion and thus lower rates of NO_2(g) generation and concomitantly higher selectivity. Interestingly, vis-aged 2.0 CdTe/P25 catalyst was still capable of preserving both its NO conversion and selectivity upon aging. Hence, increasing CdTe QD loading under vis irradiation could be an efficient strategy to extend the catalytic lifetime of the CdTe/P25 photocatalytic architecture. It is important to note that for the vis-aged samples, ultimate $DeNO_x$ index was achieved by the 2.0 CdTe/P25 sample (Figure 8b).

To understand the origin of the higher NO conversion and selectivity of CdTe/P25 composite system, comprehensive control experiments were conducted. These experiments were geared toward identifying the catalytic functionality of the individual structural components of the catalyst architecture (QD dispersant medium (i.e., H_2O)) as well as the influence of the TGA capping agent.

3.2.4. Effect of H_2O(l) on Titanium Dioxide (P25) Photocatalysis. To understand the effect of the aqueous dispersant (H_2O(l)) on the PHONOS performance of the CdTe/P25 system, fresh and aged H_2O(l)/P25 samples were prepared with the same volumes used in the CdTe/P25 preparation and tested under UV-A or vis illumination (Figures 7c,d and 8a,b). It is apparent that addition of increasing loadings of H_2O(l) increases both the NO conversion and selectively under both UV-A and vis light for the fresh catalysts. Enhancement of NO conversion and selectivity upon water addition can be attributed to the formation of surface hydroxyl/hydroxide functionalities, which may enhance both NO(g) + O_2(g) photooxidation and the storage of the photocatalytically generated NO_2 in the form of HONO(ads) or $HONO_2$(ads). Upon aging with UV-A or vis, photocatalytic trends tend to converge to that of pure P25, possibly due to photon-induced desorption of water or formation of oxygen vacancies triggering water loss or dehydroxylation of the titania surface.

It is apparent that the enhanced NO conversion observed for the TGA(aq) added P25 samples given in Figure 7e,f is most likely due to the aqueous content of TGA(aq). On the other hand, in all of the investigated H_2O(l)/P25 cases, enhancement in the selectivity due to water addition was not comparable to that of the fresh 1.0 CdTe/P25 and 2.0 CdTe/P25 samples, suggesting that the aqueous dispersant in the CdTe suspension could not be solely responsible for the boost in PHONOS performance of CdTe/P25 composite system.

3.2.5. Effect of Thioglycolic Acid Capping (TGA) on Titanium Dioxide (P25) Photocatalysis. The influence of TGA on titania photocatalysis was investigated in control experiments given in Figures 7e,f and 8a,b. In these control experiments, photocatalytic performance of both fresh and aged (under UV-A or vis) TGA(aq)/P25 samples were tested in comparison to pure P25. Data corresponding to fresh 0.1 TGA(aq)/P25 (Figure 7e) suggested that addition of TGA(aq) slightly increased the NO conversion (as will be demonstrated in the next section, the increase in NO conversion due to TGA(aq) addition on P25 was due to the enhancement provided by H_2O(l) in the TGA aqueous solution, rather than the TGA itself) along with a notable increase in selectivity under UV-A illumination. However, the selectivity for fresh 0.1 TGA(aq)/P25 was limited to ca. 50%, which was much lower compared to the fresh 1.0 CdTe/P25 catalyst (Figure 7a), where the selectivity exceeded 90%. Upon increasing the TGA(aq) loading to 0.5 mL and then dosing 0.1 mL of pure TGA, fresh TGA/P25 samples showed first a drastic fall followed by the complete loss of NO conversion under UV-A light (Figure 7e). This is consistent with the poisoning and blocking of the active sites of titania with moderate or high loadings of TGA. A similar behavior was also observed for the TGA/P25 samples aged under UV-A (Figure 7e). Analogous control experiments performed under vis illumination for fresh and vis light aged TGA/P25 catalysts (Figures 7f and 8b) revealed similar trends, although the initial rise in selectivity for the low loadings of TGA (i.e., fresh 0.1 TGA(aq)/P25) was about 70%. Thus, overall, it was observed that in the absence of CdTe, low loadings of TGA(aq) on P25 provided a minor boost in the NO conversion and a moderate rise in the selectivity. However, the rise in neither selectivity

DOI: 10.1021/acsami.8b18036
ACS Appl. Mater. Interfaces 2019, 11, 865−879

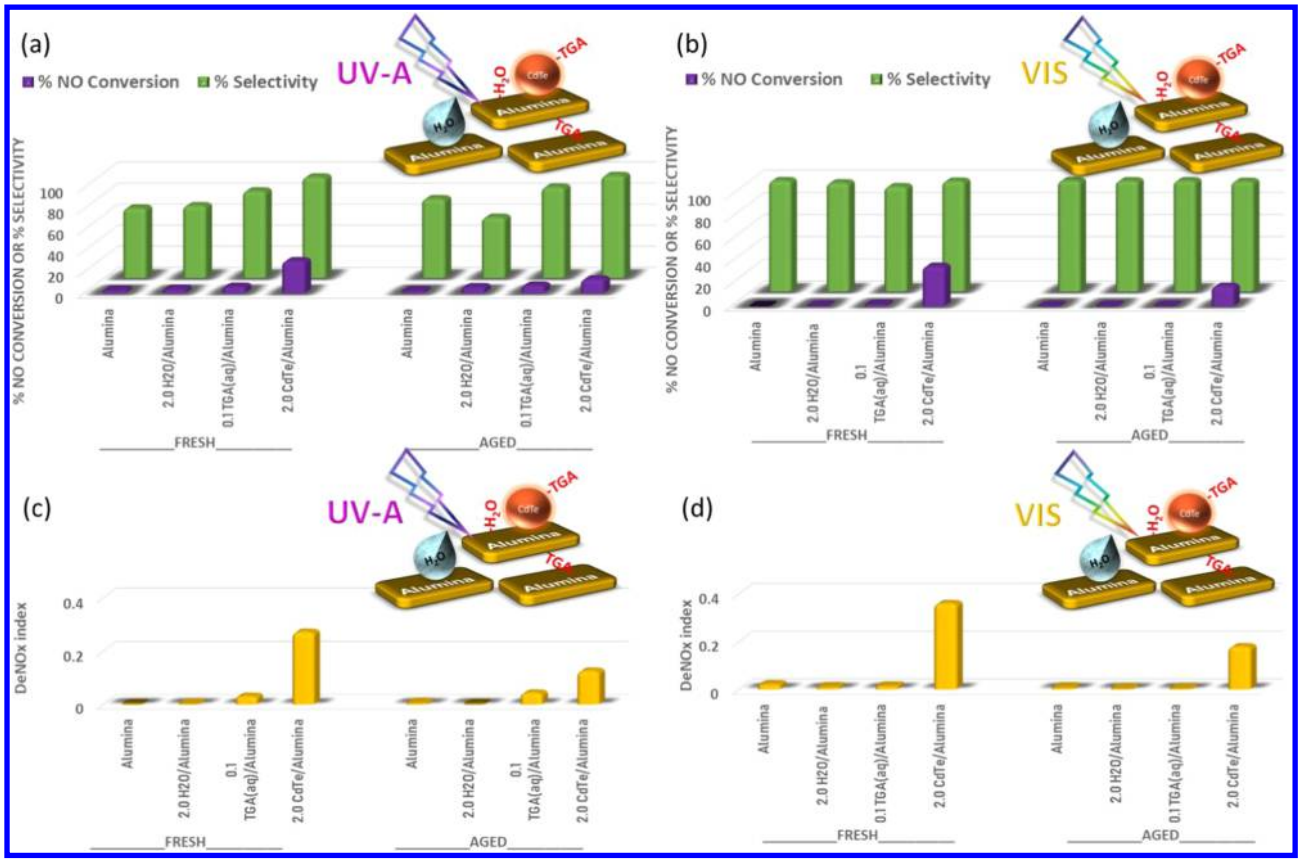

Figure 9. Photocatalytic performance results for pure alumina, 2.0 $H_2O(l)$/alumina, 0.1 TGA(aq)/alumina, and 2.0 CdTe/alumina under (a) UV-A irradiation and (b) vis irradiation. Corresponding $DeNO_x$ index values for (c) UV-A irradiation and (d) vis irradiation.

nor NO conversion did not match that of the fresh 1.0 CdTe/P25 system. Along these lines, it can be argued that TGA surface functionalities had a capability to bind to photocatalytically generated NO_2 to form $-S-R-NO_x$ surface species and enhance selectivity. Furthermore, at moderate-to-high loadings of TGA directly bound to titania, photocatalytic action of titania was first drastically hindered and then totally terminated. In other words, in the absence of CdTe, addition of only TGA(aq) or pure TGA on P25 did not lead to high enough photocatalytic performance that was observed for fresh CdTe/P25 composite system. Hence, the photocatalytic activity boost observed for the TGA-capped CdTe/P25 system cannot be solely attributed to the TGA/P25 interface nor to the TGA surface functionalities as the $DeNO_x$ index of all of the investigated TGA/P25 samples were much lower than that of the optimal CdTe/P25 catalyst (Figure 8a,b).

3.2.6. Control Experiments without Titanium Dioxide (P25). To demonstrate the intrinsic photocatalytic activity of the structural subcomponents of the CdTe/P25 system other than the titania domains, further control experiments were carried out without titania. For this purpose, γ-Al_2O_3 (S_{BET} = 200 m^2/g) was chosen as a nonphotocatalytic support material and the photocatalytic performances of pure alumina, 2.0 $H_2O(l)$/alumina, 0.1 TGA(aq)/alumina, and 2.0 CdTe/alumina were investigated (Figure 9). As expected, pure alumina, 2.0 $H_2O(l)$/alumina, and 0.1 TGA(aq)/alumina systems were completely inactive, revealing no significant photocatalytic conversion. On the other hand, both fresh and aged 2.0 CdTe/alumina samples showed notable activity under UV-A as well as vis irradiation. These observations suggest that CdTe QDs could have some contribution in both NO(g) + O_2(g) photooxidation and the storage of the photocatalytically generated NO_2 in the CdTe/P25 system, where the latter is the more prominent effect.

3.2.7. Reuse Measurements. To demonstrate the longer-term performance of the CdTe QD-functionalized titania systems, reuse experiments were performed as shown in Figures 10 and 11 under UV-A and vis illumination and were compared to those of P25. In these experiments, each catalyst was exposed to five successive photocatalytic runs, each of which lasted 60 min. As can be seen in Figure 10a, under UV-A illumination, NO conversion of P25 remained rather intact at 30%, while its already low initial selectivity of 23% further dropped to 17% after five runs. In other words, under UV-A illumination after five runs, P25 generated mostly toxic NO_2(g) species rather than performing any noteworthy amount of NO_x abatement. Under vis illumination, initial 40% NO conversion of P25 decreased to 37% after five runs while its selectivity decreased from 36 to 31%. Therefore, P25 preserved its severely negative $DeNO_x$ index in all of the reuse experiments under both UV-A and vis irradiation (Figure 11). It was apparent that 2.0 CdTe/P25 systems could significantly outperform pure P25 not only in terms of the initial performance, but also after five runs under both UV-A and vis illumination. Under UV-A illumination, initial 38% NO conversion of 2.0 CdTe/P25 decreased to 20%, while its initially high selectivity of 94% was preserved at a high level of 74% after five runs. Likewise, under vis illumination, NO conversion of 2.0 CdTe/P25 decreased from 42 to 25% after five runs, while maintaining its extremely high initial selectivity

DOI: 10.1021/acsami.8b18036
ACS Appl. Mater. Interfaces 2019, 11, 865−879

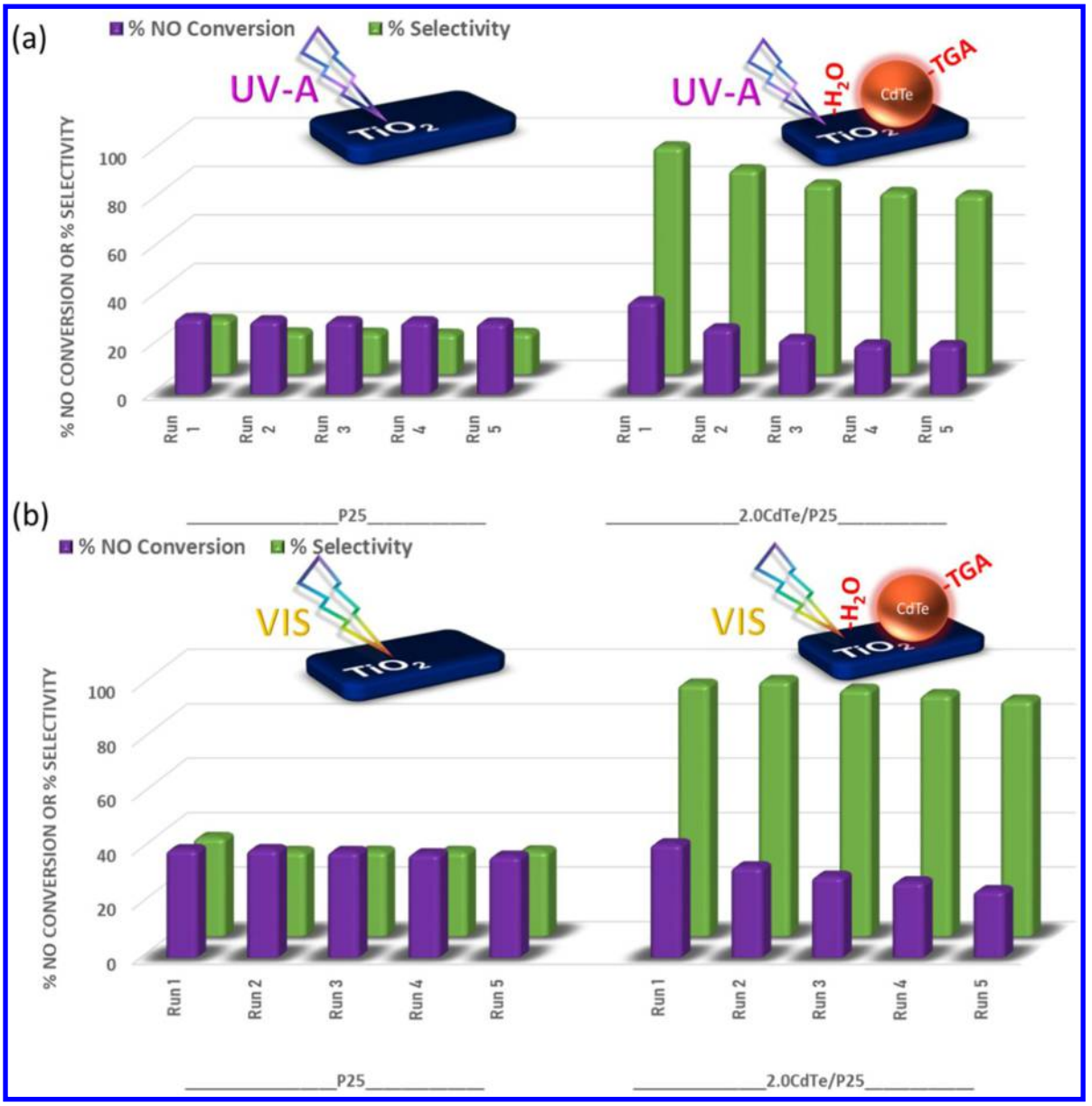

Figure 10. NO conversion and selectivity values obtained in reuse experiments for P25 and 2.0 CdTe/P25 (a) under UV-A and (b) vis light irradiation.

of 94%, revealing only a minor decrease to 84% after five runs. It is important to note that after five runs, even if the $DeNO_x$ index of 2.0 CdTe/P25 shows an attenuation, it still maintains positive $DeNO_x$ index values under both UV-A and vis irradiation, outperforming P25 (Figure 11).

3.2.8. Effect of Temperature on Titanium Dioxide (P25) Photocatalysis under Vis Light Illumination. In the currently presented photocatalytic measurements, temperature of the reactor stayed within 20−25 °C during the UV-A measurements, while it reached up to 40−45 °C during the vis light experiments. This was due to the differences in the emission spectra of the UV-A and vis light sources utilized. Thus, it was important to elucidate the contribution of thermal chemistry/catalysis and verify whether the observed catalytic enhancement under vis light illumination originated from thermal processes or photocatalytic processes. Since the thermal conductivity of the PMMA material used in the photocatalytic reactor did not allow efficient external temperature control by cooling/heating of the reactor, we decided to control the reactor temperature by changing the distance between the vis light source and the reactor. By increasing the distance between the vis light source and the reactor, vis-photon flux was decreased, which led to cooling of the reactor. Obviously, this also resulted in attenuation of the photocatalytic action. Then, photocatalytic performance of fresh 2.0 CdTe/P25 and fresh P25 samples were measured under vis light illumination at different reactor temperatures, as shown in Figure 12. Note that since the photon flux values for these different temperatures were not identical, NO conversion and selectivity values for these two temperatures were not comparable (Figure 12a).

Therefore, for the comparison of the photocatalytic activities at different temperatures and different vis flux values, we normalized the photocatalytic NO_x storage and NO_2 generation with the incident vis photon flux values and calculated the corresponding photonic efficiency values, as

DOI: 10.1021/acsami.8b18036
ACS Appl. Mater. Interfaces 2019, 11, 865−879

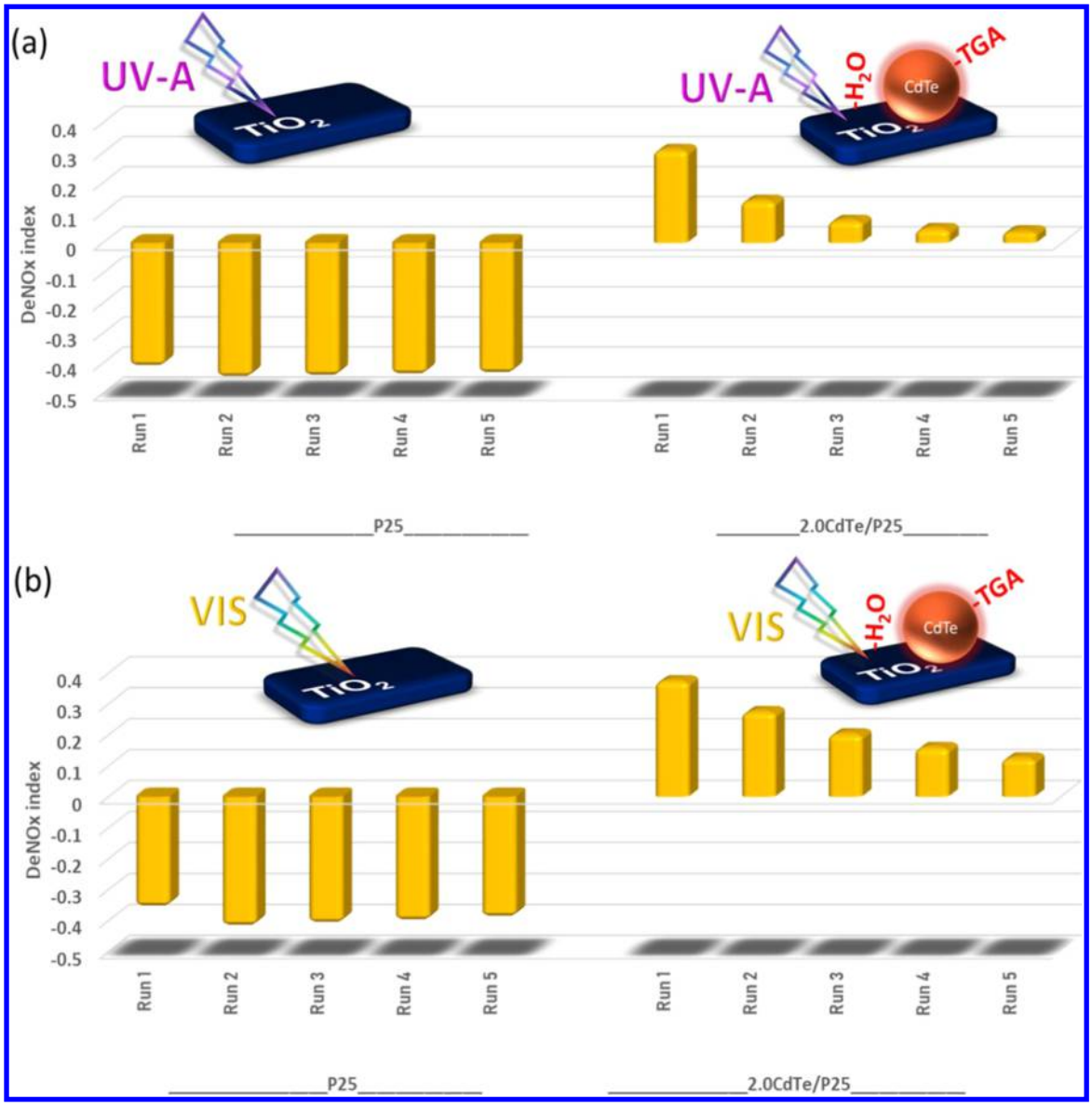

Figure 11. DeNO$_x$ index values obtained in reuse experiments for P25 and 2.0 CdTe/P25 (a) under UV-A and (b) vis light irradiation.

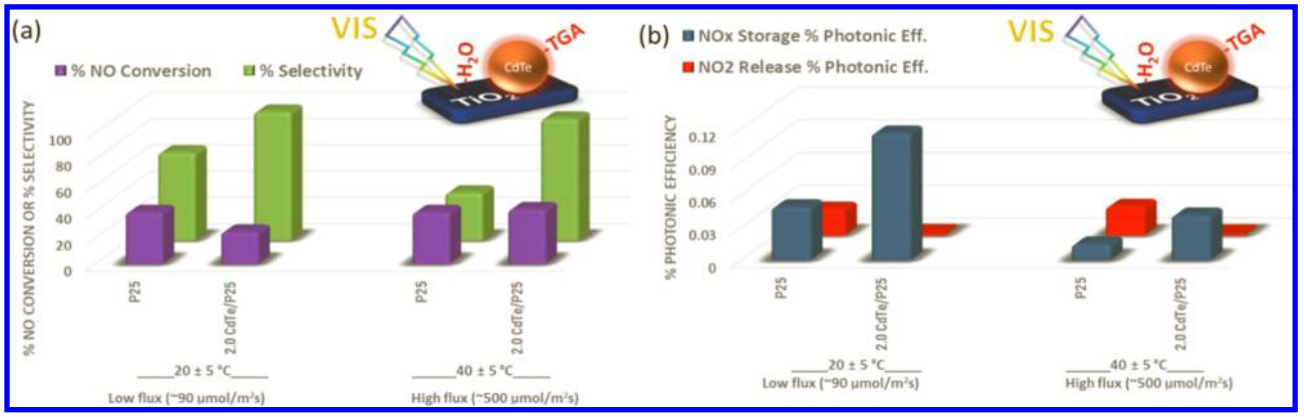

Figure 12. Temperature-dependent photocatalytic activity data for fresh P25 and 2.0 CdTe/P25 samples under vis light illumination. (a) NO conversion and selectivity data vs temperature for titanium dioxide (P25) and 2.0 CdTe/P25 under visible light. (b) Photonic efficiency vs temperature for titanium dioxide (P25) and 2.0 CdTe/P25 under visible light.

presented in Figure 12b. It can be readily seen in Figure 12b that for both pure P25 and 2.0 CdTe/P25 samples irradiated with vis light, increasing temperature had no significant influence on $NO_2(g)$ generation % photonic efficiency. On

DOI: 10.1021/acsami.8b18036
ACS Appl. Mater. Interfaces 2019, 11, 865−879

the other hand, increasing temperature significantly diminished the NO_x storage % photonic efficiency. This could be attributed to the changes in the interaction of water vapor ($H_2O(g)$) with the photocatalyst surface, alteration in the surface coverage of adsorbed water and variations in the hydroxyl/hydroxide surface concentration, which in turn modified the photocatalytic behavior. It is possible that the $H_2O(g)$ adsorption to the catalyst surface and the associated surface hydroxyl concentration could be lower at higher temperatures, which may lead to the suppression of the total photocatalytic NO_x storage at higher temperatures. As an overall result, temperature-dependent control experiments demonstrated that enhancement in PHONOS performance of the CdTe/P25 composite material under vis illumination does not result from thermal processes but mostly from the photocatalytic effects.

4. CONCLUSIONS

In the current work, we demonstrated that a composite material architecture composed of thioglycolic acid (TGA)-functionalized CdTe QDs decorated on P25 (titania) can be used as an efficient broad-band photocatalyst in photocatalytic NO_x oxidation and storage (PHONOS). We showed that this particular photocatalyst system can readily harvest both UV-A and vis light and exhibit promising photocatalytic NO_x abatement functionality toward NO(g) at room temperature. Although P25 titania benchmark photocatalyst could reveal a reasonable photocatalytic NO(g) conversion, it suffered from extremely low selectivity toward solid-state NO_x storage, rendering it an unacceptable photocatalyst for airborne NO_x emission control. In contrast, CdTe/P25 composite photocatalyst with an optimized QD loading could not only reveal a high NO(g) conversion, but it could also display an extremely high selectivity toward NO_x storage, outperforming the P25 titania commercial benchmark photocatalyst.

Through a series of comprehensive control experiments, we also investigated the individual photocatalytic functionalities of each structural component used in the TGA-CdTe/P25 composite structure. These experiments illustrated that TGA, CdTe, and titania components in the TGA-CdTe/P25 composite operated in a synergistic manner surpassing the individual functionalities of TGA, CdTe, and titania in their separated (pure) forms. We also showed that $H_2O(l)$ used as a dispersant for CdTe QDs also enhanced NO(g) conversion and selectivity.

We also investigated the stability of the TGA-CdTe/P25 system exposed to UV-A/vis illumination and extended durations of reaction conditions. These experiments illustrated some loss of photocatalytic activity and selectivity for TGA-CdTe/P25. In spite of this catalytic performance loss, TGA-CdTe/P25 could significantly surpass the overall catalytic performance of P25 titania commercial benchmark photocatalyst at all times. Increasing CdTe QD loading in the catalyst formulation revealed a trade-off between photocatalytic activity and catalyst lifetime/stability. It was shown that a slight increase in the CdTe loading from the values optimized for maximum conversion and selectivity can enhance the lifetime of the catalyst with only a minor loss in performance.

Currently proposed composite materials open a wide synthetic playground for designing new photocatalytic architectures, where chemical, electronic, optical, and catalytic properties of the composite can be fine-tuned by modifying the organic capping functionality, changing the QD type/composition/size/shape, and altering the underlying photocatalytic active metal-oxide support material. Along these lines, further studies are ongoing in our research team, where we exploit these synthetic opportunities to design enhanced photocatalytic architectures for room-temperature airborne NO_x abatement.

ASSOCIATED CONTENT

Supporting Information

The Supporting Information is available free of charge on the ACS Publications website at DOI: 10.1021/acsami.8b18036.

Schematic for the custom-made photocatalytic flow reactor; amounts of chemicals used for the preparation of CdTe(aq)/P25, $H_2O(l)$/P25 and TGA(aq)/P25; description of the photocatalytic performance calculations; optical images of the catalyst preparation stages; NO_x storage and NO_2 release % photonic efficiency results for fresh and aged; NO_x storage and NO_2 release % photonic efficiency values obtained in reuse experiments for P25 and 2.0 CdTe/P25 (PDF)

AUTHOR INFORMATION

Corresponding Authors

*E-mail: volkan@bilkent.edu.tr (H.V.D.).
*E-mail: ozensoy@fen.bilkent.edu.tr (E.O.).

ORCID

Munir Ullah Khan: 0000-0002-8033-6780
Hilmi Volkan Demir: 0000-0003-1793-112X
Emrah Ozensoy: 0000-0003-4352-3824

Present Address

⊥Advanced Catalytic Materials, KAUST Catalysis Center, King Abdullah University of Science and Technology, Thuwal 23955, Saudi Arabia (M.C.).

Notes

The authors declare no competing financial interest.

ACKNOWLEDGMENTS

E.O. acknowledges the scientific collaboration with TARLA project founded by the Ministry of Development of Turkey (project code: DPT2006K-120470). H.V.D. is grateful to the support from TUBA. The authors acknowledge SASOL Ltd. for providing Puralox SBA200 γ-Al_2O_3 materials.

REFERENCES

(1) Roy, S.; Baiker, A. NO_x Storage−Reduction Catalysis: from Mechanism and Materials Properties to Storage−Reduction Performance. *Chem. Rev.* **2009**, *109*, 4054−4091.

(2) Epling, W. S.; Campbell, L. E.; Yezerets, A.; Currier, N. W.; Parks, J. E. Overview of the Fundamental Reactions and Degradation Mechanisms of NO_x Storage/Reduction Catalysts. *Catal. Rev.* **2004**, *46*, 163−245.

(3) Herreros, J.; George, P.; Umar, M.; Tsolakis, A. Enhancing Selective Catalytic Reduction of NO_x with Alternative Reactants/Promoters. *Chem. Eng. J.* **2014**, *252*, 47−54.

(4) Liu, H.; Chaney, J.; Li, J.; Sun, C. Control of NO_x Emissions of a Domestic/Small-Scale Biomass Pellet Boiler by Air Staging. *Fuel* **2013**, *103*, 792−798.

(5) Lu, W.; Olaitan, A. D.; Brantley, M. R.; Zekavat, B.; Erdogan, D. A.; Ozensoy, E.; Solouki, T. Photocatalytic Conversion of Nitric oxide on Titanium Dioxide: Cryotrapping of Reaction Products for online Monitoring by Mass Spectrometry. *J. Phys. Chem. C* **2016**, *120*, 8056−8067.

DOI: 10.1021/acsami.8b18036
ACS Appl. Mater. Interfaces 2019, 11, 865−879

(6) Polat, M.; Soylu, A. M.; Erdogan, D. A.; Erguven, H.; Vovk, E. I.; Ozensoy, E. Influence of the Sol−Gel Preparation method on the Photocatalytic NO Oxidation Performance of TiO_2/Al_2O_3 Binary Oxides. *Catal. Today* **2015**, *241*, 25−32.
(7) Erdogan, D. A.; Polat, M.; Garifullin, R.; Guler, M. O.; Ozensoy, E. Thermal Evolution of Structure and Photocatalytic Activity in Polymer Microsphere Templated TiO_2 Microbowls. *Appl. Surf. Sci.* **2014**, *308*, 50−57.
(8) Soylu, A. M.; Polat, M.; Erdogan, D. A.; Say, Z.; Yıldırım, C.; Birer, Ö.; Ozensoy, E. $TiO_2−Al_2O_3$ Binary Mixed Oxide Surfaces for Photocatalytic NO_x Abatement. *Appl. Surf. Sci.* **2014**, *318*, 142−149.
(9) Yang, L.; Hakki, A.; Wang, F.; Macphee, D. E. Different roles of Water in Photocatalytic $DeNO_x$ Mechanisms on TiO_2: Basis for Engineering Nitrate Selectivity? *ACS Appl. Mater. Interfaces* **2017**, *9*, 17034−17041.
(10) Henderson, M. A. A Surface Science Perspective on TiO_2 Photocatalysis. *Surf. Sci. Rep.* **2011**, *66*, 185−297.
(11) Luttrell, T.; Halpegamage, S.; Tao, J.; Kramer, A.; Sutter, E.; Batzill, M. Why is Anatase a better Photocatalyst than Rutile?-Model Studies on Epitaxial TiO_2 Films. *Sci. Rep.* **2014**, *4*, No. 4043.
(12) Yu, J.; Yu, J. C.; Leung, M. K.-P.; Ho, W.; Cheng, B.; Zhao, X.; Zhao, J. Effects of Acidic and Basic Hydrolysis Catalysts on the Photocatalytic Activity and Microstructures of Bimodal Mesoporous Titania. *J. Catal.* **2003**, *217*, 69−78.
(13) Tay, Q.; Liu, X.; Tang, Y.; Jiang, Z.; Sum, T. C.; Chen, Z. Enhanced Photocatalytic Hydrogen Production with Synergistic two-Phase Anatase/Brookite TiO_2 Nanostructures. *J. Phys. Chem. C* **2013**, *117*, 14973−14982.
(14) Beltrán, A.; Gracia, L.; Andrés, J. Density Functional Theory Study of The Brookite Surfaces and Phase Transitions between Natural Titania Polymorphs. *J. Phys. Chem. B* **2006**, *110*, 23417−23423.
(15) Gázquez, M. J.; Bolívar, J. P.; Garcia-Tenorio, R.; Vaca, F. A Review of the Production Cycle of Titanium Dioxide Pigment. *Mater. Sci. Appl.* **2014**, *05*, 441.
(16) Bourikas, K.; Kordulis, C.; Lycourghiotis, A. Titanium Dioxide (Anatase and Rutile): Surface Chemistry, Liquid−Solid Interface Chemistry, and Scientific Synthesis of Supported Catalysts. *Chem. Rev.* **2014**, *114*, 9754−9823.
(17) Lang, X.; Ma, W.; Chen, C.; Ji, H.; Zhao, J. Selective Aerobic Oxidation Mediated by TiO_2 Photocatalysis. *Acc. Chem. Res.* **2014**, *47*, 355−363.
(18) Schneider, J.; Matsuoka, M.; Takeuchi, M.; Zhang, J.; Horiuchi, Y.; Anpo, M.; Bahnemann, D. W. Understanding TiO_2 Photocatalysis: Mechanisms and Materials. *Chem. Rev.* **2014**, *114*, 9919−9986.
(19) Daghrir, R.; Drogui, P.; Robert, D. Modified TiO_2 for Environmental Photocatalytic Applications: A Review. *Ind. Eng. Chem. Res.* **2013**, *52*, 3581−3599.
(20) Zhang, H.; Banfield, J. F. Structural Characteristics and Mechanical and Thermodynamic Properties of Nanocrystalline TiO_2. *Chem. Rev.* **2014**, *114*, 9613−9644.
(21) Colmenares, J. C.; Luque, R. Heterogeneous Photocatalytic Nanomaterials: Prospects and Challenges in Selective Transformations of Biomass-Derived Compounds. *Chem. Soc. Rev.* **2014**, *43*, 765−778.
(22) Zhang, J.; Zhou, P.; Liu, J.; Yu, J. New Understanding of The Difference of Photocatalytic Activity among Anatase, Rutile and Brookite TiO_2. *Phys. Chem. Chem. Phys.* **2014**, *16*, 20382−20386.
(23) Hüsken, G.; Hunger, M.; Brouwers, H. J. H. Experimental Study of Photocatalytic Concrete Products for Air Purification. *Build. Environ.* **2009**, *44*, 2463−2474.
(24) Rahim, S.; Ghamsari, M. S.; Radiman, S. Surface Modification of Titanium Oxide Nanocrystals with PEG. *Sci. Iran.* **2012**, *19*, 948−953.
(25) Devahasdin, S.; Fan, C., Jr.; Li, K.; Chen, D. H. TiO_2 Photocatalytic Oxidation of Nitric Oxide: Transient Behavior and Reaction Kinetics. *J. Photochem. Photobiol., A* **2003**, *156*, 161−170.
(26) Duan, Y.; Luo, J.; Zhou, S.; Mao, X.; Shah, M. W.; Wang, F.; Chen, Z.; Wang, C. TiO_2-Supported Ag Nanoclusters with Enhanced Visible Light Activity for the Photocatalytic Removal of NO. *Appl. Catal., B* **2018**, *234*, 206−212.
(27) Momeni, M. M.; Ghayeb, Y. Fabrication, Characterization and Photoelectrochemical Behavior of Fe−TiO_2 Nanotubes Composite Photoanodes for Solar Water Splitting. *J. Electroanal. Chem.* **2015**, *751*, 43−48.
(28) Chen, Y.; Wang, Y.; Li, W.; Yang, Q.; Hou, Q.; Wei, L.; Liu, L.; Huang, F.; Ju, M. Enhancement of Photocatalytic Performance with the use of Noble-Metal-Decorated TiO_2 Nanocrystals as Highly Active Catalysts for Aerobic Oxidation under Visible-Light Irradiation. *Appl. Catal., B* **2017**, *210*, 352−367.
(29) Yu, Q.; Ballari, M. M.; Brouwers, H. Indoor Air Purification using Heterogeneous Photocatalytic Oxidation. Part II: Kinetic Study. *Appl. Catal., B* **2010**, *99*, 58−65.
(30) Li, X.; Wang, D.; Cheng, G.; Luo, Q.; An, J.; Wang, Y. Preparation of Polyaniline-Modified TiO_2 Nanoparticles and their Photocatalytic Activity under Visible Light Illumination. *Appl. Catal., B* **2008**, *81*, 267−273.
(31) Fischer, K.; Gawel, A.; Rosen, D.; Krause, M.; Latif, A. A.; Griebel, J.; Prager, A.; Schulze, A. Low-Temperature Synthesis of Anatase/Rutile/Brookite TiO_2 Nanoparticles on a Polymer Membrane for Photocatalysis. *Catalysts* **2017**, *7*, 209.
(32) Hensel, J.; Wang, G.; Li, Y.; Zhang, J. Z. Synergistic effect of CdSe Quantum Dot Sensitization and Nitrogen Doping of TiO_2 Nanostructures for Photoelectrochemical Solar Hydrogen Generation. *Nano Lett.* **2010**, *10*, 478−483.
(33) Bajorowicz, B.; Nadolna, J.; Lisowski, W.; Klimczuk, T.; Zaleska-Medynska, A. The effects of Bifunctional Linker and Reflux Time on the Surface Properties and Photocatalytic Activity of CdTe Quantum Dots Decorated $KTaO_3$ Composite Photocatalysts. *Appl. Catal., B* **2017**, *203*, 452−464.
(34) Bajorowicz, B.; Kobylański, M. P.; Gołąbiewska, A.; Nadolna, J.; Zaleska-Medynska, A.; Malankowska, A. Quantum Dot-Decorated Semiconductor Micro-and Nanoparticles: A Review of their Synthesis, Characterization and Application in Photocatalysis. *Adv. Colloid Interface Sci.* **2018**, *256*, 352−372.
(35) Ohtani, B.; Prieto-Mahaney, O.; Li, D.; Abe, R. What is Degussa (Evonik) P25? Crystalline Composition Analysis, Reconstruction from Isolated Pure Particles and Photocatalytic Activity Test. *J. Photochem. Photobiol., A* **2010**, *216*, 179−182.
(36) Rui, Z.; Wu, S.; Peng, C.; Ji, H. Comparison of TiO_2 Degussa P25 with Anatase and Rutile Crystalline Phases for Methane Combustion. *Chem. Eng. J.* **2014**, *243*, 254−264.
(37) Raj, K.; Viswanathan, B. Effect of Surface Area, Pore Volume and Particle Size of P25 Titania on the Phase Transformation of Anatase to Rutile. *Indian J. Chem., Sect. A* **2009**, *48*, 1378−1382.
(38) Wang, G.; Xu, L.; Zhang, J.; Yin, T.; Han, D. Enhanced Photocatalytic Activity of Powders (P25) via Calcination Treatment. *Int. J. Photoenergy* **2012**, *2012*, No. 265760.
(39) Sigma-Aldrich. Titanium (IV) Oxide, Nanopowder, 21 nm Primary Particle Size (TEM), ≥99.5% Trace Metals Basis. http://www.sigmaaldrich.com/catalog/product/aldrich/718467?lang=en&region=TR.
(40) Su, R.; Bechstein, R.; Sø, L.; Vang, R. T.; Sillassen, M.; Esbjornsson, B.; Palmqvist, A.; Besenbacher, F. How the Anatase-to-Rutile Ratio Influences the Photoreactivity of TiO_2. *J. Phys. Chem. C* **2011**, *115*, 24287−24292.
(41) Bickley, R. I.; Gonzalez-Carreno, T.; Lees, J. S.; Palmisano, L.; Tilley, R. J. A Structural Investigation of Titanium Dioxide Photocatalysts. *J. Solid State Chem.* **1991**, *92*, 178−190.
(42) Hurum, D. C.; Agrios, A. G.; Gray, K. A.; Rajh, T.; Thurnauer, M. C. Explaining the Enhanced Photocatalytic Activity of Degussa P25 Mixed-Phase TiO_2 using EPR. *J. Phys. Chem. B* **2003**, *107*, 4545−4549.
(43) Li, G.; Richter, C. P.; Milot, R. L.; Cai, L.; Schmuttenmaer, C. A.; Crabtree, R. H.; Brudvig, G. W.; Batista, V. S. Synergistic effect between Anatase and Rutile TiO_2 Nanoparticles in Dye-Sensitized Solar Cells. *Dalton Trans.* **2009**, *45*, 10078−10085.

DOI: 10.1021/acsami.8b18036
ACS Appl. Mater. Interfaces 2019, 11, 865−879

(44) Kho, Y. K.; Iwase, A.; Teoh, W. Y.; Mädler, L.; Kudo, A.; Amal, R. Photocatalytic H_2 Evolution over TiO_2 Nanoparticles. The Synergistic effect of Anatase and Rutile. *J. Phys. Chem. C* **2010**, *114*, 2821−2829.
(45) Bojinova, A.; Kralchevska, R.; Poulios, I.; Dushkin, C. Anatase/Rutile TiO_2 Composites: Influence of the Mixing Ratio on the Photocatalytic Degradation of Malachite Green and Orange II In Slurry. *Mater. Chem. Phys.* **2007**, *106*, 187−192.
(46) Rogach, A. L.; Franzl, T.; Klar, T. A.; Feldmann, J.; Gaponik, N.; Lesnyak, V.; Shavel, A.; Eychmüller, A.; Rakovich, Y. P.; Donegan, J. F. Aqueous Synthesis of Thiol-Capped CdTe Nanocrystals: State-of-the-Art. *J. Phys. Chem. C* **2007**, *111*, 14628−14637.
(47) Mills, A.; Elouali, S. The Nitric Oxide ISO Photocatalytic Reactor System: Measurement of NO_x Removal Activity and Capacity. *J. Photochem. Photobiol., A* **2015**, *305*, 29−36.
(48) Kisch, H.; Bahnemann, D. Best Practice in Photocatalysis: Comparing Rates or Apparent Quantum Yields? *J. Phys. Chem. Lett.* **2015**, *6*, 1907−1910.
(49) Standardization, I.O.F. *Fine Ceramics (Advanced Ceramics, Advanced Technical Ceramics)—Test Method for Air-Purification Performance of Semiconducting Photocatalytic Materials—Part 1: Removal of Nitric Oxide*; International Organization for Standardization, 2007.
(50) Yang, S.-S.; Ren, C.-L.; Zhang, Z.-Y.; Hao, J.-J.; Hu, Q.; Chen, X.-G. Aqueous Synthesis of CdTe/CdSe Core/Shell Quantum Dots as Ph-Sensitive Fluorescence Probe for the Determination of Ascorbic Acid. *J. Fluoresc. Chem.* **2011**, *21*, 1123−1129.
(51) Yan, M.; Zhang, Y.; Xu, K.; Fu, T.; Qin, H.; Zheng, X. An in vitro Study of Vascular Endothelial Toxicity of CdTe Quantum Dots. *Toxicology* **2011**, *282*, 94−103.
(52) Zhao, Y.; Wang, X.; Wu, Q.; Li, Y.; Wang, D. Translocation and Neurotoxicity of CdTe Quantum Dots in RMEs Motor Neurons in Nematode *Caenorhabditis elegans*. *J. Hazard. Mater.* **2015**, *283*, 480−489.
(53) Marchelek, M.; Grabowska, E.; Klimczuk, T.; Lisowski, W.; Zaleska-Medynska, A. Various types of Semiconductor Photocatalysts Modified by CdTe QDs and Pt NPs for Toluene Photooxidation in the Gas Phase under Visible Light. *Appl. Surf. Sci.* **2017**, *393*, 262−275.
(54) Xing, M.; Shen, F.; Qiu, B.; Zhang, J. Highly-Dispersed Boron-Doped Graphene Nanosheets Loaded with TiO_2 Nanoparticles for Enhancing CO_2 Photoreduction. *Sci. Rep.* **2014**, *4*, No. 6341.
(55) Kubelka, P. Ein Beitrag Zur Optik Der Farbanstriche (Contribution to the Optic of Paint). *Z. Tech. Phys.* **1931**, *12*, 593−601.
(56) Tauc, J. Optical Properties and Electronic Structure of Amorphous Ge and Si. *Mater. Res. Bull.* **1968**, *3*, 37−46.
(57) Li, D.; Wang, S.; Wang, J.; Zhang, X.; Liu, S. Synthesis of CdTe/TiO_2 Nanoparticles and their Photocatalytic Activity. *Mater. Res. Bull.* **2013**, *48*, 4283−4286.
(58) Adegoke, O.; Park, E. Y. Size-Confined Fixed-Composition and Composition-Dependent Engineered Band Gap Alloying Induces Different Internal Structures in L-Cysteine-Capped Alloyed Quaternary CdZnTeS Quantum Dots. *Sci. Rep.* **2016**, *6*, No. 27288.
(59) Valden, M.; Lai, X.; Goodman, D. W. Onset of Catalytic Activity of Gold Clusters on Titania with the Appearance of Nonmetallic Properties. *Science* **1998**, *281*, 1647−1650.
(60) Yu, W. W.; Qu, L.; Guo, W.; Peng, X. Experimental Determination of the Extinction Coefficient of CdTe, CdSe, and CdS Nanocrystals. *Chem. Mater.* **2003**, *15*, 2854−2860.
(61) Bloh, J. Z.; Folli, A.; Macphee, D. E. Photocatalytic NO_X Abatement: Why the Selectivity Matters. *RSC Adv.* **2014**, *4*, 45726−45734.
(62) Ozensoy, E.; Peden, C. H.; Szanyi, J. Model NO_x Storage Systems: Storage Capacity and Thermal Aging of BaO/Θ-Al_2O_3/NiAl (100). *J. Catal.* **2006**, *243*, 149−157.
(63) Hummatov, R.; Gülseren, O. U.; Ozensoy, E.; Toffoli, D.; Üstünel, H. First-Principles Investigation of NO_X And SO_X Adsorption on Anatase-Supported BaO and Pt Overlayers. *J. Phys. Chem. C* **2012**, *116*, 6191−6199.
(64) Kayhan, E.; Andonova, S. M.; Şentürk, G. K. S.; Chusuei, C. C.; Ozensoy, E. Fe Promoted NO_X Storage Materials: Structural Properties and NO_X Uptake. *J. Phys. Chem. C* **2010**, *114*, 357−369.
(65) Andonova, S. M.; Şentürk, G. K. S.; Ozensoy, E. Fine-Tuning the Dispersion and the Mobility of BaO Domains on NO_X Storage Materials via TiO_2 Anchoring Sites. *J. Phys. Chem. C* **2010**, *114*, 17003−17016.
(66) Say, Z.; Vovk, E. I.; Bukhtiyarov, V. I.; Ozensoy, E. Influence of Ceria on the NO_x Reduction Performance of NO_x Storage Reduction Catalysts. *Appl. Catal., B* **2013**, *142−143*, 89−100.
(67) Say, Z.; Mihai, O.; Tohumeken, M.; Ercan, K. E.; Olsson, L.; Ozensoy, E. Sulfur-Tolerant BaO/ZrO_2/TiO_2/Al_2O_3 Quaternary Mixed Oxides for DeNO_X Catalysis. *Catal. Sci. Technol.* **2017**, *7*, 133−144.
(68) Say, Z.; Dogac, M.; Vovk, E. I.; Kalay, Y. E.; Kim, C. H.; Li, W.; Ozensoy, E. Palladium Doped Perovskite-Based NO Oxidation Catalysts: The Role of Pd and B-Sites for NO_x Adsorption behavior via In-Situ Spectroscopy. *Appl. Catal., B* **2014**, *154−155*, 51−61.

DOI: 10.1021/acsami.8b18036
ACS Appl. Mater. Interfaces 2019, 11, 865−879